β-Disubstituted Pentacene Derivatives: Thin Film Structural Properties and Four-Probe Field Effect Mobility

Mouaad-Yassine Aliouat[a, e], Filadelfo Cristiano[a], Lydia Abbassi[e, f], Stéphanie Escoubas[e], Fabien Mesnilgrente[a], Ludovic Salvagnac[a], Michal Šámal[b], Jiří Rybáček[b], Ludmilla Sturm[c], André Gourdon[d], Andrej Jančařík*[c], Isabelle Séguy*[a]

[a] Dr. M-Y Aliouat, Dr. F. Cristiano, F. Mesnilgrente, L. Salvagnac, Dr. I. Séguy
LAAS-CNRS, Université de Toulouse, UPS
31031 Toulouse, France
E-mail: iseguy@laas.fr

[b] Dr. M. Šámal, Dr. J. Rybáček
Institute of Organic Chemistry and Biochemistry of the Czech Academy of Sciences
166 10 Prague 6, Czech Republic

[c] Dr. L. Sturm, Dr. A. Jančařík
Univ. Bordeaux, CNRS-CRPP, UMR 5031
33600 Pessac, France
E-mail: andrej.jancarik@crpp.cnrs.fr

[d] Dr. A. Gourdon
CEMES-CNRS,
29 Rue J. Marvig, 31055 Toulouse, France

[d] Pr. S. Escoubas
Aix Marseille Université, CNRS, IM2NP
Marseille, France

[e] L. Abbassi
Aix Marseille Université, CNRS, CINaM
Marseille, France

Abstract: 2,9- and 2,10-diphenylpentacene were synthesized by direct C-H borylation of ketal-protected pentacene, followed by halodeboronation, resolution of the dihalo isomers, Suzuki arylation, cleavage of the ketals and decarbonylation in the solid state. They were studied as main active components in organic field effect transistors (OFETs). Diphenyl substitution of pentacene affects the unit cell dimensions only slightly, preserving a face to edge molecular packing in the first layers of thin films evaporated on SiO_2 substrates. Both isomers self-assemble into nanoribbons during the thin film growth upon vapor deposition. The similarity between the surface induced phases of the 2,9-isomer and unsubstituted pentacene leads to similar 4-probe hole mobilities, i.e. 0.13 $cm^2V^{-1}s^{-1}$ for the former. Whereas 2,9-disubstitution thus does essentially preserve the thin film characteristics of unsubstituted pentacene, 2,10-disubstitution is detrimental to the molecular ordering in the thin films and therefore to the field effect mobility which is only 0.07 $cm^2V^{-1}s^{-1}$. The known strong enhancement of field effect mobility observed upon diphenyl substitution of anthracene can thus not be emulated analogously with pentacene.

Introduction

[n]Acenes are planar polycyclic aromatic hydrocarbons consisting of linearly fused benzene rings. The smallest member of the family is anthracene, with three benzene rings connected in a row. Linear elongation by further benzene annulations leads to a systematic decrease of the HOMO-LUMO gap and of the reorganization energy. These decreases lead to very high charge carrier mobilities as required for organic electronics.[1] For example, tetraphenyl-tetracene (rubrene) and pentacene have become benchmark organic semiconductors for thin film OFETs. Pentacene and hexacene have been intensively studied as chromophores with low-laying triplet states singlet fission.[2–4] Unfortunately, the reactivity of acenes increases with increasing length, because acenes longer than pentacene are of partial open shell character in their ground state. This diradical character of long acenes suggests applicability in spintronics[5] and plasmonics[6,7].

The derivatization of acenes by attaching large functional groups to their peripheries is one of the most versatile methods for their stabilization[8,9] and for the tuning of their electronic properties. Attached substituents significantly increase the solubility, which is a necessary parameter for processing techniques using inks, and play important role in the crystal engineering.[10] The derivatization of anthracene has led to a remarkable improvement of the charge carrier mobility in organic single crystal transistors (OSCTs) as well as in OFETs compared to anthracene itself.[11] 2,6-Diphenyl anthracene (DPA) has one of the highest charge mobilities among organic semiconductors (Figure 1).[12] Improved mobilities have also been demonstrated upon derivatization of tetracene.[13]

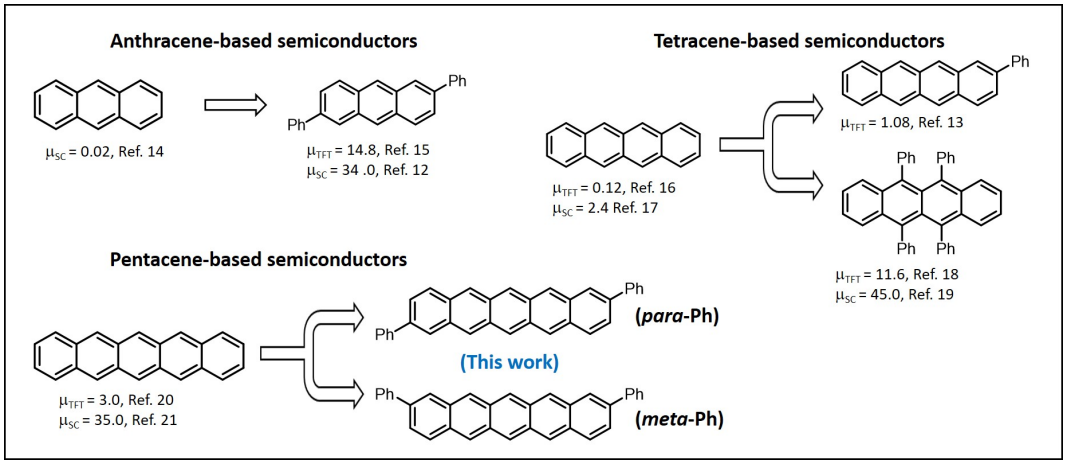

Figure 1. Charge transport mobilities of acene-based semiconductors, μ_{SC} are mobilities of single crystal, μ_{TFT} are mobilities of thin film, mobilities are in $\mu = cm^2V^{-1}s^{-1}$.

For acenes longer than tetracene, direct functionalization is a formidable challenge due to their high reactivity and poor solubility. However, in recent years, appreciable progress has been made in developing of soluble and stable acene precursors, which can be converted in the final step thermally or photochemically to the corresponding acenes in quantitative yields without any non-volatile by-products.[1] This elegant precursor approach has triggered the investigation of the charge transport mobilities in longer acenes than pentacene.[22–24] However, the aromatic functionalization of longer acenes than tetracene for the purpose of studying the evolution of their semiconducting properties has been neglected. Thus, we have focused here on the synthesis of the simplest 2,9- and 2,10-diaryl-substituted pentacenes, i.e. the diphenyl derivatives, and their performance in OFETs. They are of particular interest as they bear the phenyl substituents in the sterically less congested *β* positions, allowing stronger conjugation than the corresponding α homologs substituted in 1,8 or 1,11. For simplicity, we call the 2,9-disubstituted derivatives "***para-"*** and their 2,10 analogs ***"meta-"***.

Results and Discussion

Easy access to ketal-protected pentacene precursor[25] **1** enables us to investigate the direct Ir-catalyzed diborylation of **1** (Scheme 1). The reaction of **1** with bis(pinacolato)diboron in the presence of an iridium catalyst provided a 1:1 mixture of the boronic ester substituted pentacene ketals ***para*-Bpin** and ***meta*-Bpin**. Unfortunately, the identical retention factor (Rf) on silica gel of the two isomers did not allow us to obtain them individual in pure form. However, transformation to the corresponding bromides (***para-*/*meta*-Br**) or iodides (***para-*/*meta*-Br**) leads to differentiation of the Rf, enabling efficient separation by HPLC or continuous chromatography. These dihalogen pentacene derivatives ***para-*/*meta*-X** are useful building blocks for the regiospecific synthesis of acene-containing polycyclic arenes and, potentially, acene-based polymers.

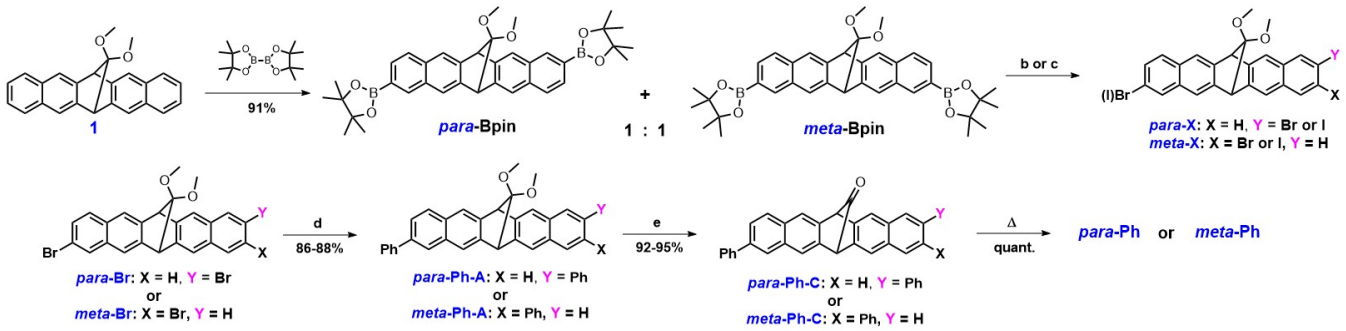

Scheme 1. a) B_2pin_2 (2.2 eq.), [*Ir*(cod)(OMe)]$_2$ (5 mol%), dtbbpy (10 mol%) 65 °C, 24 h, 91%; b) $CuBr_2$ (8.0 eq.), 90°C, 18 h, 92%; c) NIS (2.2 eq.), 80°C, 18 h, 60%; d) phenylboronic acid (2.2 eq.), K_2CO_3 (4.0 eq.), $Pd(PPh_3)Cl_2$, 85°C, 3 h, 88% for ***para*-Ph-A** and 86% for ***meta*-Ph-A**; e) TMSI (4.0 eq.), 25°C, 16 h, 95% for ***para*-Ph-C** and 92% for ***meta*-Ph-C**; f) neat, 200°C.

Two-fold Suzuki-Miyaura cross-coupling of ***para*-Br** or ***meta*-Br** with phenylboronic acid, followed by the hydrolysis of the ketal groups, afforded carbonyl-protected diphenylpentacenes ***para*-Ph-C** and ***meta*-Ph-C** as a stable colorless compounds. The conversion of these to the final diphenylpentacenes was monitored by thermal gravimetric analysis (for details, see Supporting Information). A weight loss of 6.6% for *para* and 6.5% for *meta* (calcd. 6.8%), accompanied by a color change from white to purple, occurred at 180°C and 187°C, respectively. The absorption spectra of ***para*-/*meta*-Ph** were collected in 1,1,2,2,-tetrachloroethane at room temperature under inert conditions (for details, see Supporting Information, page S17). In the UV-vis absorption spectra, the pentacene subunit with its characteristic structured bands (511, 549 and 596 nm), identical for both isomers, was observed. The absorption maxima λ_{max} were bathochromically shifted by 18 nm relative to unsubstituted pentacene (495, 530 and 578 nm)[26], testifying to the extension of the π-conjugation.

Thin films of each diphenylpentacene were prepared: ***Para*-** and ***meta*-Ph-C** (see scheme 1) were first deposited into Knudsen cells in a Plassys MEB 550B chamber at 2.10^{-7} mbar. After thermal decarbonylation, films of ***para*-** and ***meta*-Ph** were grown by sublimation without any substrate heating. The deposition rates and film thicknesses were controlled by a vibrating quartz thickness monitor placed next to the sample holder. For shortest diphenylanthracenes (DPAs), particularly high hole mobilities (μ_{TFT}) of 10 $cm^2V^{-1}s^{-1}$ were reported for very low growth rates of 0.05 Å/s[15], therefore we opted here for the same deposition rate. To investigate the effect of the diphenyl functionalization of pentacene on the charge transport, we used ***para*-** and ***meta*-Ph** as semiconducting layers in bottom-gate/bottom-contact (BG/BC) OFETs. Devices were fabricated on bare n-type Si/SiO_2 substrates and Cr/Au contacts according to the process described in our previous work.[24] We adapted here to thin film OFETs the particular four-probe gated device geometry developed on single crystal devices by H.H. Choi *et al.*[27] The OFET structure includes additional voltage probes (with varying width t = 10 to 40 µm) placed on the side of the channel in four distinct devices disposed on the same substrate (as illustrated in figure SI-1 (b)). This geometry was designed to evaluate any possible shunting effect caused by the probes used to sense the voltage in the transistor channel. Device characterizations were performed in the dark at room temperature (see SI). The output $I_D(V_D)$ and transfer $I_D(V_G)$ characteristics at small drain voltage (V_{DS}=-2V and -5V, linear regime) are shown in figure 2. According to the output curves, all devices behave as p-type transistors that saturate at high drain-source voltage (V_{DS}), with higher drain-source current (I_{DS}) for OFETs using the *para* isomer ***para*-Ph**.

The devices display negligible hystereses and linear transfer curves above V_G = -40V due to a large contact resistance.[28] Field effect ($\mu_{TFT\text{-}lin}/\mu_{TFT\text{-}sat}$) and four-probe ($\mu_{TFT\text{-}4p}$) charge carrier mobilities were extracted from the transfer curves in saturation and linear regimes via a linear fitting of the transconductance and from the slope of the $(I_D)^{1/2}$ versus V_G slope (see figure SI-2).

***Para*-Ph** shows device performances similar to pentacene, with $\mu_{TFT\text{-}lin}$ off 5.7 x 10^{-2} $cm^2V^{-1}s^{-1}$ and 5.2 x 10^{-2} $cm^2V^{-1}s^{-1}$, on/off ratios of 6.6 x 10^3 and 1.1 x 10^4 (between gate voltage of 0V and -50V) and threshold voltages of -4.7 V and 6 V, respectively, whereas ***meta*-Ph** exhibits inferior values (see table 1). For all studied OFETs, a good match is observed between the mobilities obtained from the linear and saturation regimes ($\mu_{TFT\text{-}lin} \approx \mu_{TFT\text{-}sat}$), indicating a low concentration of traps in the transistor channel.[28] $\mu_{TFT\text{-}lin/sat}$ is different from the extracted $\mu_{TFT\text{-}4p}$, corroborating a significant contact resistance. This is to be expected in bottom contact OFET devices where the OSC structural properties may be modified at the *metal*/organic interfaces.[29] The average $\mu_{TFT\text{-}4p}$ obtained from six devices based on ***para*-Ph** and ***meta*-Ph** are 0.14 $cm^2V^{-1}s^{-1}$ and 0.06 $cm^2V^{-1}s^{-1}$ respectively. $\mu_{0\text{-}FET\text{-}4p}$ corresponding to a vanishing probe width (t = 0) was extrapolated from the linear fits of $\mu_{FET\text{-}4p}$ vs probe size (figure 3).

Table 1. Electrical parameters of OFETs extracted from transfer characteristics (fig. 2 and SI) in linear (V_{DS} = -5V) and saturated (V_{DS} = -50 V) regimes.

Samples	V_{th} (V)	I_{on} / I_{off}	μ_{lin} ($cm^2.V^{-1}.s^{-1}$)	μ_{sat} ($cm^2.V^{-1}.s^{-1}$)	μ_{4p} ($cm^2.V^{-1}.s^{-1}$) [b]	$\mu_{0\text{-}4p}$ ($cm^2.V^{-1}.s^{-1}$)
Pentacene[a]	- 6	1.1 x 10^4	5.2 x 10^{-2}	5 x 10^{-2}	0.13	0.099
***Para*-Ph**	- 4.7	6.6 x 10^3	5.7 x 10^{-2}	5.1 x 10^{-2}	0.13 (0.14)	0.1
***Meta*-Ph**	- 5.9	2.5 x 10^4	1.6 x 10^{-2}	1.7 x 10^{-2}	0.07 (0.06)	0.039

[a] For pentacene output and transfer curves see figure SI-3-a and SI-3-b respectively. [b] Values within brackets are the average values of 6 devices.

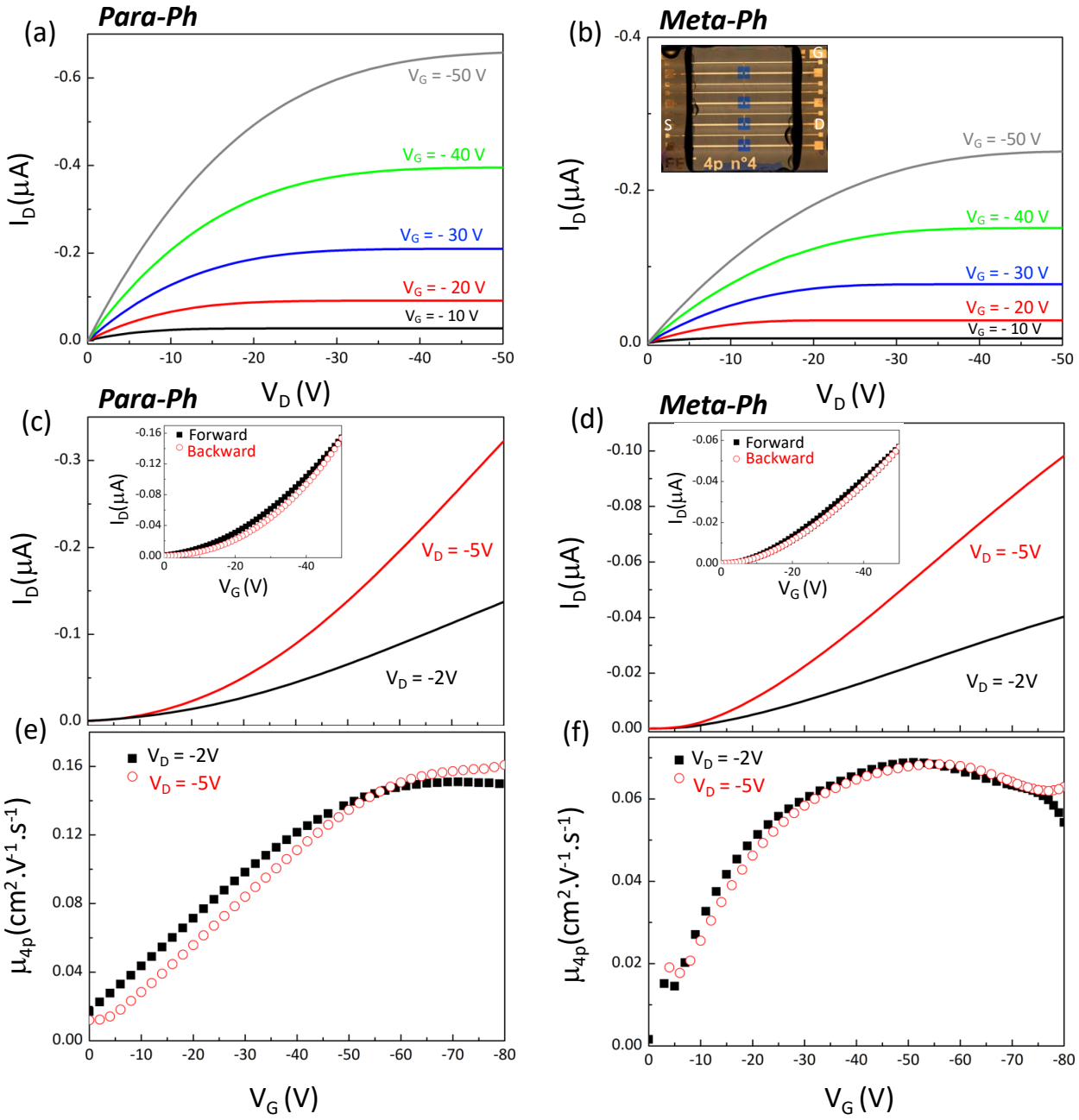

Figure 2. *Characteristics of **para-/meta-Ph** BC/BG OFETs: output curves for (a) **para-Ph** and (b) **meta-Ph** (inset shows the devices) sublimated at 0.05 Å/s; linear regime transfer curves for (c) **para-Ph** and (d) **meta-Ph** (inset shows the transfer hystereses for V_{DS} = -5V); 4-probe mobility calculated from Eq.2 (see S.I.) vs gate voltage for V_{DS} = -2V and -5V for (e) **para-Ph** and (f) **meta-Ph**. Device parameters: channel length L= 240 µm, channel width W= 300 µm, probe length D=80 µm, probe width t=30 µm, the gate dielectric is 225 nm-thick thermally grown SiO_2 with C_{ox}=15.3.10^{-9} F.cm^{-2}.*

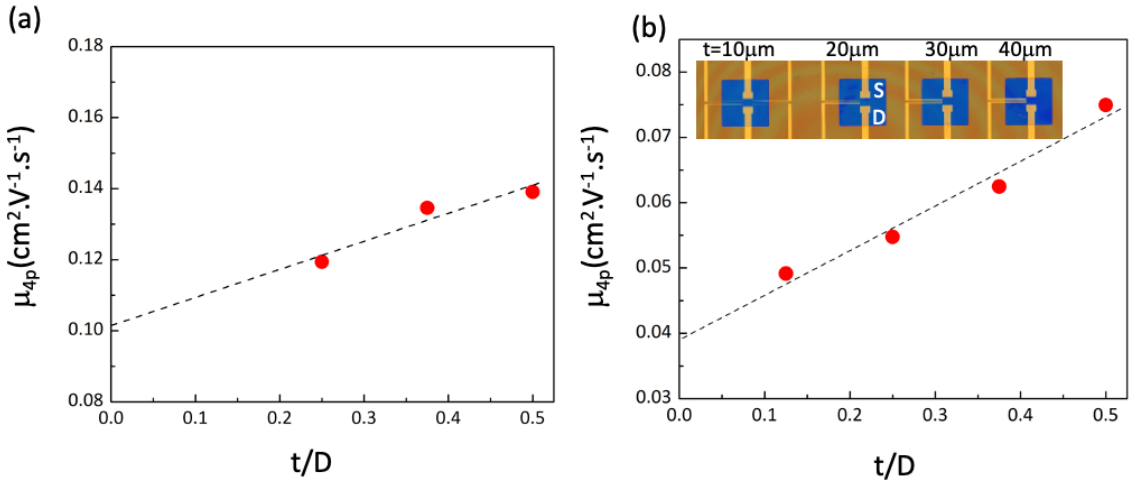

Figure 3. *Four-gate probe mobilities vs probe size for (a)* ***para-Ph*** *and (b)* ***meta-Ph*** *OFETs ($\mu_{FET\text{-}4p}$ vs t/D for pentacene is shown in SI-4) .*

In all OFETs, $\mu_{FET\text{-}4p}$ increased with the probe size and becomes slightly overestimated for the largest probes. From the $\mu_{FET\text{-}lin}$, $\mu_{FET\text{-}sat}$ and $\mu_{0\text{-}FET\text{-}4p}$ values, it emanates that the charge mobility in ***meta*-Ph** OFETs does not reach the values of pentacene and ***para*-Ph** OFETs.

To explore the thin film structures and their influence on μ_{FET}, atomic force microscopy (AFM), grazing incidence X-ray diffraction (GIXD; at the ESRF synchrotron radiation facility at beamline BM02 in Grenoble, France), and transmission electron microscopy (TEM) analyses were carried out. For those experiments, samples were prepared on additional substrates included in the deposition chamber during device preparation.

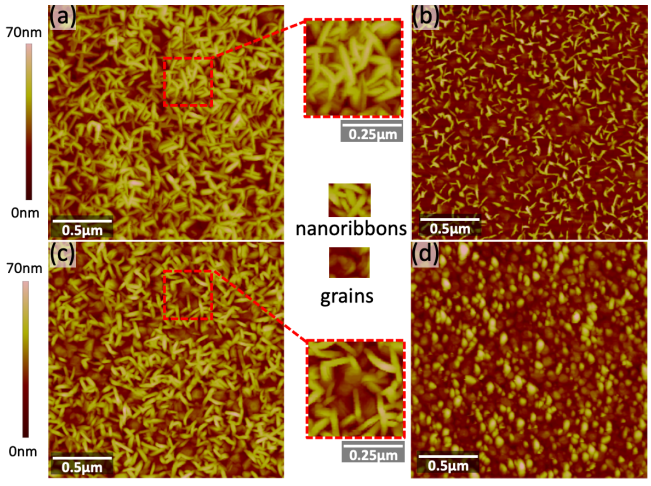

Figure 4. *AFM topography of 50 nm (a) and 15 nm (b) thick* ***para-Ph*** *films and (c) 50 nm and (d) 15 nm thick* ***meta-Ph*** *films sublimated at 0.05 Å/s.*

The AFM images in Figure 4 show the diphenylpentacenes deposited on SiO_2. The layers consist of entangled nanoribbons, leading to a high rms surface roughness (10.4 nm for ***para*-Ph**, 7 nm for ***meta*-Ph**). Surprisingly, these structures differ strongly from the ones observed for pentacene films deposited in the same conditions, which are made of three-dimensional islands (see figure SI-6). When the film thickness is reduced to a few nm, the nanoribbons vanish, and a surface mostly constituted of small grains appears (see figures 4 b and d). This indicates that the nanoribbon formation does not occur during the first steps of the film growth. The molecular arrangement into nanoribbons probably appears after the early stage of deposition once interactions between substrate and molecules weaken, regardless of the position of the phenyl groups (*para*- or *meta*-). In addition, the AFM topological pictures reveal that 2,9-disubstitution of pentacene (*para*) seems to favor the generation of nanoribbons with higher density than 2,10-disubstitution (*meta*). However, nanoribbons do not contribute to the charge transport in our device configuration (as verified with 15 nm thick ***para*-Ph** OFET see output curves figure SI-5), since it is confined in the first monolayers close to the gate oxide.

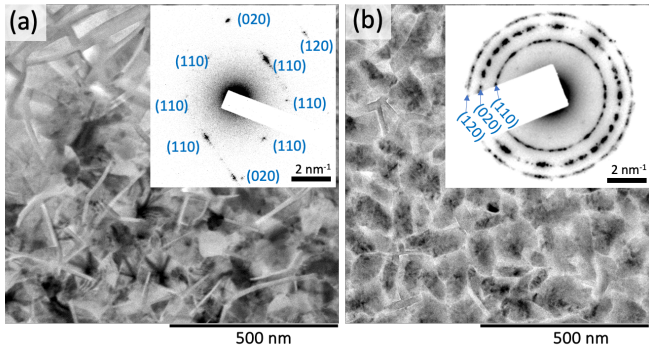

Figure 5. *(a) TEM optical micrograph of a polycrystalline* ***para-Ph*** *thin film and (b) a* ***meta-Ph*** *polycristalline thin film. The corresponding ED patterns, taken from single crystalline (a) and polycristalline regions (b) of the films are inset.*

For TEM investigations the samples have been prepared on amorphous carbon substrates mounted onto a fine-mesh grid. AFM observations confirm that the layers grown on carbon substrates have the same morphology as the ones obtained on SiO_2 (see figure SI-7), as reported for pentacene.[30] TEM images with corresponding electron diffraction (SAED) patterns are shown in figure 5.

From the SAEDs displayed in figures 5.a and 5.b, spacings of 4 Å, 4.8 Å and 7.6 Å for ***para*-Ph** and 4 Å, 4.8 Å and 6.8 Å for ***meta*-Ph** were identified. By comparing these values to those already determined for TFP of pentacene,[22] we conclude that the observed SAEDs in ***para*-/*meta*-Ph** originate from the grains (see fig. 4). For ***para*-Ph**, the SAED pattern (Fig. 5.a) shows the existence of monocrystalline zones, whereas ***meta*-Ph** features only polycristalline areas (Fig. 5.b). Thus the 2,10-phenyl substitution of pentacene leads to a loss of order at the sub-micrometer scale. Upon extended irradiation of the films, the polycristalline phase becomes amorphous, highlighting grain-boundaries (see figure SI-8). Those radiation damages induced by high-energy electrons are similar to those reported for pentacene.[32] However, for ***para*-Ph**, the nanoribbons remained unaltered after prolonged exposure to the electron beam. Those nanoribbons thus have a robust crystalline structure with self-assembled molecules, similar to what was observed for pentacene after mechanical rubbing.[30]

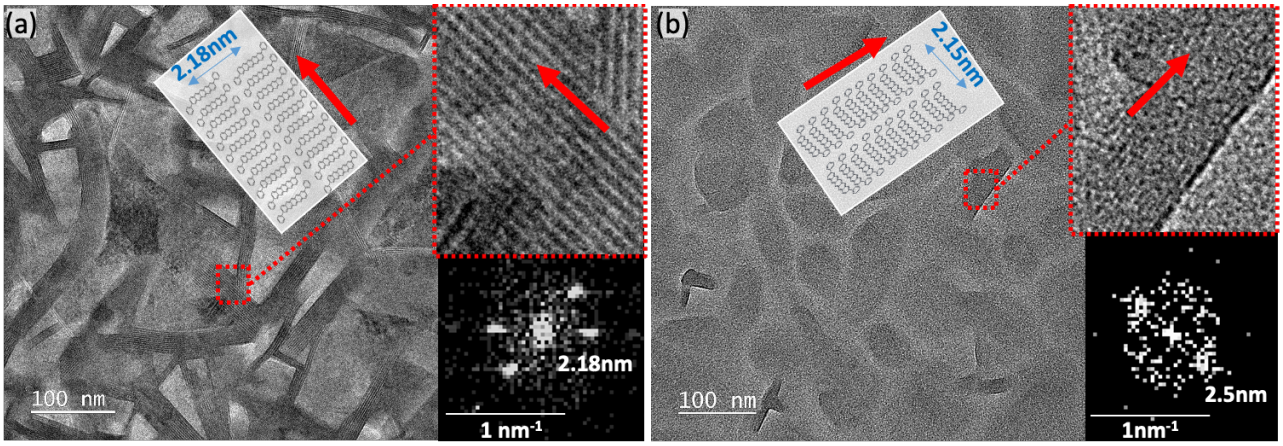

Figure 6. *In-plane TEM micrographs image of (a) para-Ph (b) , upper and lower insets: zoomed selected area with corresponding FFT pattern indicating spacing with a schematic view of the molecular order*

To evaluate distances in those molecular lattices we used a fast-Fourier-transform (FFT) from a selected area (indicated by dashed red rectangles in figure 6). Distances of 21.8 Å and 25 Å were determined for ***para*-Ph** and ***meta*-Ph** respectively. As the molecular length is about 23 Å, we can consider that, in nanoribbons, molecules are assembled with the long axis of the molecule parallel to the substrate, as drawn schematically in figure 6.

GIXD characterizations have been conducted on thin films deposited on SiO_2 substrates. As shown in figure 7 on out-of-plane (OOP) and in-plane (IP) GIXD line profiles, all the investigated samples are polycrystalline with mainly edge-on oriented molecules (see figure 7.d), as revealed by a strong *00l* peak series along the OOP direction (Fig. 7.a) and a noticeable 110 peak along the IP direction in the diffraction patterns (Fig. 7.c). The OOP line profiles (q_z) display a set of doubled peaks (see inset Fig. 7.a) demonstrating the polymorphic structure of the films with two distinct phases: a surface induced thin film phase (TFP) and a bulk phase (BP).[33] On the basis of the relative intensity of the out-of-plane d_{001} peaks, it can be verified that 2,10-diphenyl substitution of pentacene leads to the loss of order in thin films, concordant with TEM. Interplanar spacings of d_{001} (TFP) = 15.5 Å and d_{001} (BP) = 14.8 Å were extracted for pentacene which means that the molecules are slightly tilted from the surface normal by θ_{TFP}=6.49° and by θ_{BP}=23.79°in the TFP and BP respectively.

After its diphenyl functionalization, we can clearly see a shift of the 001-peak in the lower q range, indicative of a rise of d_{001} accompanying the increase of the length of the molecules. The extracted out-of-plane d_{001} values for TFP and BP are 22.7 Å and 22.3 Å for ***para*-Ph** and 23.4 Å and 22.8 Å for ***meta*-Ph**, indicating in greater tilts from those determined for pentacene. Those tilts were estimated at $\theta_{TFP\text{-}para\text{-}Ph}$ = 25.27° and $\theta_{BP\text{-}para\text{-}Ph}$ =36.07° and $\theta_{TFP\text{-}meta\text{-}Ph}$ = 21.22° and $\theta_{BP\text{-}meta\text{-}Ph}$ = 34.22° (see Figure 7 d) and might contribute to the molecular self-assembly in the ***para*-/*meta*-Ph** bulk phase. Figure 7b shows in-plane (q_{xy}) 001 peaks that are only present for ***para*-/*meta*-Ph**. These peaks are attributed to the nanoribbons where molecules are organized as displayed in figure 7d with in plane $d_{001\text{-}para\text{-}Ph}$ of 22.7 Å and $d_{001\text{-}meta\text{-}Ph}$ of 23.4 Å. GIXD measurements performed on 15nm thick layers do not evidence any in-plane 001 peak, confirming that the nanoribbons do not form during the initial stages of the film growth (see figure SI-11). Figure 7c shows that in-plane GIXD patterns (intensity vs q_{xy}) exhibit many of the same peaks (and d_{110}, d_{020}, and d_{120} spacings see table 2) for ***para*-/*meta*-Ph** and for the benchmark pentacene sample.

Those results suggest that, for the thin film phase, the principal dissimilarity between pentacene and functionalized pentacene lies in the out-of-plane spacing d_{001} and in the molecular inclination of the molecules within the (001) plane. M. Klues and *al.*[35] have shown that pentacene-like organic semiconductors exhibiting a uniform electric potential surrounding the molecule

tend to adopt a herringbone packing due to strong C-H---π interactions. Since diphenyl functionalization on the pentacene backbone will not change the electric potential at the periphery of the molecules, we can assume that a herringbone arrangement is also favored for ***para*-Ph** and ***meta*-Ph**. So for both functionalized pentacenes, at the unit cell scale the TFP displays a face to edge herringbone stacking of the molecules, with a molecular packing that is nearly identical to that of pentacene[36,37] as drawn in figure 7e. Therefore, for pentacene the diphenyl substitution does not cause an increase of the intralayer packing density, contrary to DPA where a face to face herringbone packing with d_{001} shorter than in anthracene was reported.[11] At the thin film scale, TFP similarities in pentacene and ***para*-Ph** explain the similar performance of the respective OFET devices, whereas the 2,10-diphenyl substitution causes a reduction in the field effect mobility correlated to a lower degree of out-of-plane thin film ordering.

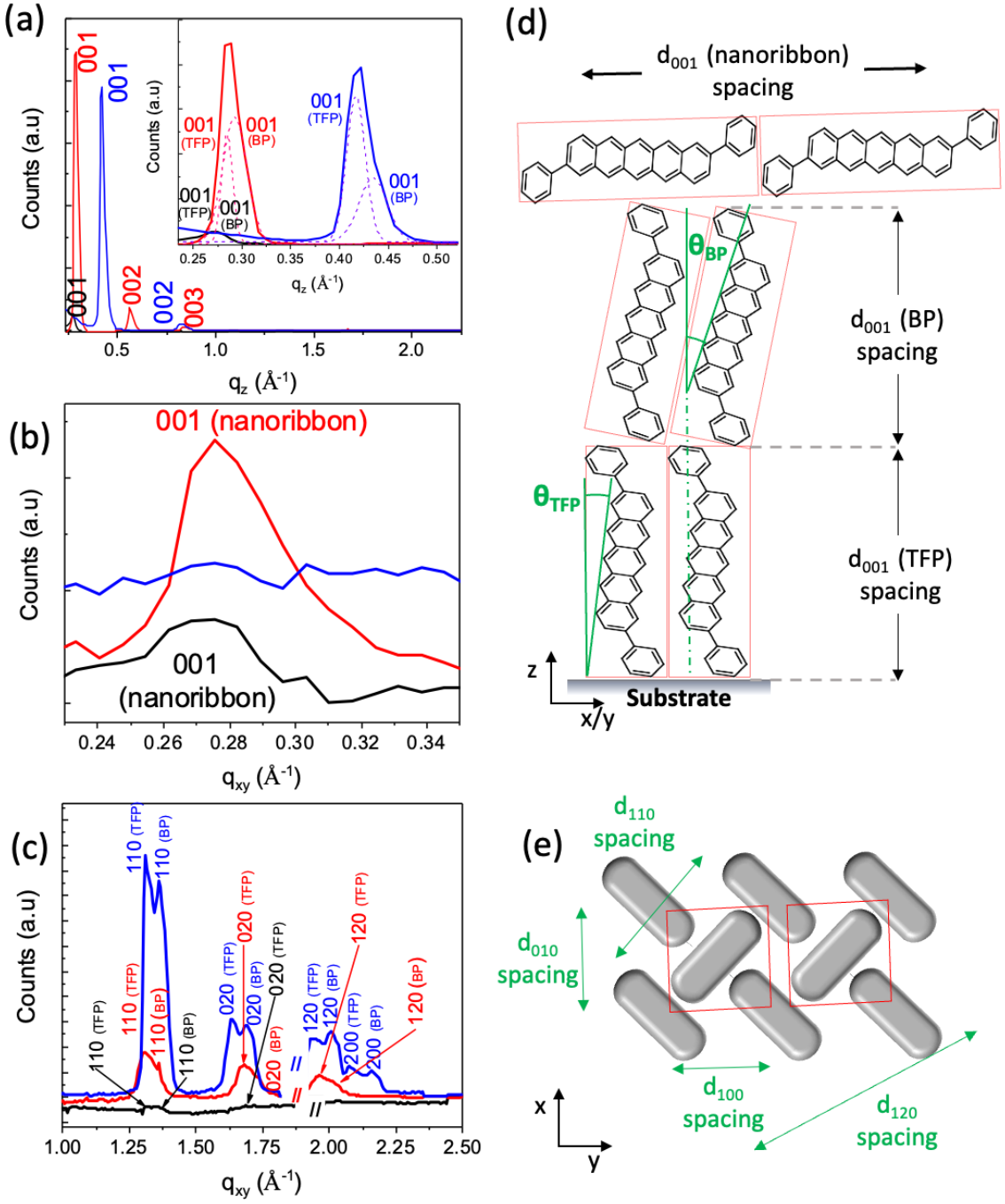

Figure 7. *(a) Out-of-plane GIXD line profiles (in-set : zoom on doubled 001 peaks), and in-plane, (b) enlarged 001peaks (c) the remaining peaks of* ***para*-***(red)/****meta*-*Ph*(black) and pentacene (blue) (d) corresponding schematic view of* ***para*-Ph** *out-of-plane molecular organization with* θ_{TFP}, θ_{BP} *tilts relative to the surface normal in TFB and BP respectively (e) corresponding schematic top view of the unit cell organization showing different interplanar spacings.*

Table 2. Comparison between lattice parameters of pentacene, *para*- and *meta*-pentacene via GIXD and TEM.

Sample[l]	GIXD d(Å)		TEM d(Å)	Assigned to
	TFP	BP	TFP	
Pentacene	15.5 - (15.4 [34])	14.8 - (14.1 [34])	N.A.	001 (OOP)
	N.A.	N.A.	N.A.	001 (IP)
	4.79 - (4.65 [34])	4.6 - (4.63 [34])	4.95 - (4.95 [32])	110 (IP)
	7.66 - (7.54 [34])	7.4 - (7.8 [34])	7.8	020 (IP)
	4.21	3.13 - (3.1 [34])	3.3 - (3.1 [34])	120 (IP)
	6.04 - (5.94 [34])	5.84 - (6.09 [34])	5.85	200 (IP)
***Para*-Ph**	22.7	22.3	N.A.	001 (OOP)
	22.7 [a]	N.A.	21.8 (FFT)	001 (IP)
	4.79	4.62	4.8	110 (IP)
	7.48	7.25	7.6	020 (IP)
	3.2	3.11	4	120 (IP)
	N.A.	N.A.	N.A.	200 (IP)
***Meta*-Ph**	23.4	22.8	N.A.	001 (OOP)
	23.4	N.A.	25 (FFT)	001 (IP)
	5.52	4.64	4.8	110 (IP)
	7.54	7.3	6.8	020 (IP)
	N.A.	N.A.	4	120 (IP)
	N.A.	N.A.	N.A.	200 (IP)

[a] Values in red represent the nanoribbons.

Conclusion

In summary, we have developed a synthetic strategy to *β*-substituted pentacenes which opens the door to regioregular acene-based polyaromatic hydrocarbons and, potentially, polymers. Furthermore, we have demonstrated that the diphenyl extension of the pentacene π-conjugation does not lead to an enhancement of the field effect mobility as observed between anthracene and DPA. The reason is that *β*-functionalization of pentacene with phenyl groups, does not influence sufficiently the intermolecular interactions and the edge-to-face orientation between pentacene cores. This reflects that phenyl groups are significantly smaller with weaker intermolecular interactions than the pentacene units. For this reason, functionalization of shorter acenes such as anthracene or tetracene can significantly alter the intrinsic edge-to-face packing of acene units and lead to more efficient intermolecular orientations. Thereby substituted anthracenes or tetracenes can surpass longer acenes like pentacene in the field effect mobility. We have shown experimentally that the unit cells of pentacene and of both diphenyl pentacenes exhibit similarly close molecular packing. We have observed formation of nanoribbons due to molecular self-assembly during growth of the bulk phase of the films. The OFET characteristics combined with the structural thin film studies have evidenced that the "*meta*" functionalization of pentacene is detrimental to the molecular ordering and therefore to the field effect mobility, whereas "*para*" functionalization is not.

Experimental Section

General

The acene precursors **1** was prepared by our previously reported method.[1] Otherwise, all commercially available solvents, catalysts, and reagent grade materials were used as received.

Syntheses

Irridium-mediated direct borylation of acene precursor 1: In a typical experiment, a well dried Schlenk flask was charged with acene precursor 1 (100 mg, 0.284 mmol, 1 equiv.), bis(pinacolato)diboron (159 mg, 0.624 mmol, 2.2 equiv.), (1,5-Cyclooctadiene)(methoxy)iridium(I) dimer (9.4 mg, 14.2 µmol, 5 mol%) and ligand 4,4′-Di-tert-butyl-2,2′-dipyridyl (7.6 mg, 28.4 µmol, 10 mol%), flushed with nitrogen and anhydrous THF (6 mL) was injected. The resulting reaction mixture was stirred under inert atmosphere at 65°C overnight. After cooling to rt, the solvent was evaporated under the reduced pressure and the residue was purified by chromatography on silica gel (hexane-ethyl acetate 5:1) to afford inseparable mixture of ***para*-Bpin/*meta*-Bpin** (156 mg, 91%) as a white amorphous solid.

Conversion of pinacolboronates (*para*-Bpin/*meta*-Bpin) to the corresponding bromo-derivatives *para*-Br/*meta*-Br: In a pressure tube the regioisomers mixture 1a/1b (100 mg, 0.165 mmol) was dissolved in a Mixture of solvents THF-MeOH(1.5 mL, 1:3). Then a solution of CuBr2 (296 mg, 1.32 mmol, 8 equiv.) in water (4.5 mL) was added and the reaction mixture was bubbled with nitrogen for 10 min and then it was heated to 90 °C and stirred at this temperature overnight. After that, the mixture was diluted with water (5 ml) and extracted with dichloromethane (3 × 5 ml). The combined organic portions were dried over anhydrous MgSO4. The solvents were removed in vacuo to get pure mixture of regioisomers *para*-Br and *meta*-Br which were separated by HPLC or by continuous chromatography, for details see supporting information.

Conversion of pinacolboronates to the corresponding iodo-derivatives *para*-I/*meta*-I: A pressure tube was charged with mixture of regioisomers 1a/1b (100 mg, 0.165 mmol), CuI (70 mg, 0.364 mmol, 2.2 equiv.) and N-iodosuccinimide (82 mg, 0.364 mmol, 2.2 equiv.) and anhydrous mixture of solvents of DMF-Toluene (9mL, 2:1). The reaction mixture was degassed and then it was heated to 80 °C and stirred at this temperature overnight. After cooling to rt, the solvents were removed in vacuo and the residue was purified by flash chromatography on silica gel (toluene) to afford pure mixture of regioisomers *para*-I and *meta*-I, which were separated by HPLC or by continuous chromatography, for details see supporting information.

2,9-Dibromo-15,15-dimethoxy-6,13-dihydro-6,13-methanopentacene *para*-Br

Obtained as a white amorphous solid. (88% yield after separation)
^{1}H NMR (400 MHz, $CDCl_3$): 3.23 (s, 6H), 4.71 (s, 2H), 7.45 (dd, J = 8.7, 2.0, 2H), 7.58 (bd, J = 8.7, 2H), 7.62 (s, 2H), 7.68 (s, 2H), 7.86 (dd, J = 2.0, 0.8, 2H). ^{13}C NMR (101 MHz, $CDCl_3$): 51.43, 54.90, 119.56, 119.83, 120.68, 124.99, 128.94, 129.44, 129.92, 131.13, 133.85, 143.42, 144.02. IR ($CHCl_3$): 3060 w, 3041 w, 2963 w, 2835 w, 1597 m, 1491 m, 1460 w, sh, 1418 w, 1257 m, 1175 w, 1097 s, 1067 m, 913 m, 902 m, 887 w, 810 w, 649 w, 568 w, 476 w cm^{-1}. EI MS: 510 ($M^{+\bullet}$, 11), 436 (100), 356 (11), 276 (33), 138 (17).HR EI MS: calcd for $C_{25}H_{18}O_2{}^{79}Br_2$ 507.9668, found 507.9666.

2,10-Dibromo-15,15-dimethoxy-6,13-dihydro-6,13-methanopentacene *meta*-Br

Obtained as a white amorphous solid. (84% yield after separation)
^{1}H NMR (400 MHz, $CDCl_3$): 3.23 (s, 6H), 4.70 (d, J = 1.7, 1H), 4.71 (d, J = 1.6, 1H), 7.45 (dd, J = 8.7, 2.0, 2H), 7.57 (bd, J = 8.7, 2H), 7.63 (s, 2H), 7.67 (s, 2H), 7.87 (d, J = 2.0, 2H). ^{13}C NMR (101 MHz, $CDCl_3$): 51.43, 54.87, 54.92, 119.55, 119.90, 120.61, 124.99, 128.95, 129.41, 129.95, 131.13, 133.84, 143.40, 144.04. IR ($CHCl_3$): 3063 w, 3042 w, 2963 w, 2835 w, 1597 m, 1491 m, 1459 w, 1419 w, 1256 m, 1175 w, 1097 s, 1069 m, 915 m, 902 m, 884 w, 810 w, 650 w, 572 w, 476 w cm^{-1}. EI MS: 510 ($M^{+\bullet}$, 7), 436 (100), 356 (11), 276 (33), 138 (19). HR EI MS: calcd for $C_{25}H_{18}O_2{}^{79}Br_2$ 507.9668, found 507.9665.

2,9-Diiodo-15,15-dimethoxy-6,13-dihydro-6,13-methanopentacene *para*-I

Obtained as a white amorphous solid. (84% yield after separation)
^{1}H NMR (400 MHz, $CDCl_3$): 3.22 (s, 6H), 4.69 (s, 2H), 7.44 (d, J = 8.6, 2H), 7.58 (s, 2H), 7.62 (dd, J = 8.6, 1.8, 2H), 7.66 (s, 2H), 8.09 (d, J = 1.7, 2H). ^{13}C NMR (101 MHz, $CDCl_3$): 51.42, 54.93, 91.07, 119.62, 120.69, 124.97, 129.43, 131.49, 134.20, 134.34, 136.52, 143.62, 143.77. IR ($CHCl_3$): 3061 vw, 2962 w, 2835 w, 1591 m, 1487 m, 1460 w, 1444 w, 1416 w, 1256 s, 1178 w, 1165 w, 1158 w, 1097 vs, 1059 w, 1033 w, 641 w, 634 w, 568 w, 475 m cm^{-1}. APCI MS: 605 ($[M+H]^+$). HR APCI MS: calcd for $C_{25}H_{19}O_2I_2$ 604.9469, found 604.9463.

2,10-Diiodo-15,15-dimethoxy-6,13-dihydro-6,13-methanopentacene *meta*-I

Obtained as a white amorphous solid. (67% yield after separation)
^{1}H NMR (400 MHz, $CDCl_3$): 3.22 (s, 6H), 4.69 (d, J = 1.7, 1H), 4.70 (d, J = 1.6, 1H), 7.43 (d, J = 8.6, 2H), 7.59 (s, 2H), 7.61 (dd, J = 8.6, 1.8, 2H), 7.65 (s, 2H), 8.09 (d, J = 1.8, 2H). ^{13}C NMR (101 MHz, $CDCl_3$): 51.42, 54.93, 91.07, 119.68, 120.63, 124.97, 129.40, 131.49, 134.21, 134.34, 136.55, 143.55, 143.83. IR ($CHCl_3$): 3060 vw, 2962 w, 2835 w, 1590 m, 1487 m, 1459 w, 1444 w, 1416 w, 1256 s, 1176 w, 1170 w, 1158 w, 1097 vs, 1059 w, 1033 w, 641 w, 635 w, 568 w, 475 m cm^{-1}. APCI MS: 605 ($[M+H]^+$). HR APCI MS: calcd for $C_{25}H_{19}O_2I_2$ 604.9469, found 604.9463.

15,15-Dimethoxy-2,9-diphenyl-6,13-dihydro-6,13-methanopentacene *para*-Ph-

A pressure tube was charged with *para*-Br (200 mg, 0.39 mmol), phenylboronic acid (105 mg, 0.86 mmol, 2.2 equiv.), potassium carbonate (216 mg, 1.56 mmol, 4.0 equiv), Pd(PPh3)2Cl2 (14.0 mg, 0.02 mmol, 5 mol%), toluene (4 mL), ethanol (4 mL), and water (1 mL). The mixture was bubbled with nitrogen for 10 min and then it was heated to 85 °C and stirred at this temperature for 3 h. Then, the mixture was evaporated under reduced pressure and the residue was purified by flash chromatography on silica gel (hexane-ethyl acetate 100:1 to 20:1) to afford *para*-Ph-A (173 mg, 88%) as a white amorphous solid.
^{1}H NMR (400 MHz, $CDCl_3$): 3.27 (s, 6H), 4.75 (s, 2H), 7.32 – 7.37 (m, 2H), 7.42 – 7.48 (m, 4H), 7.62 – 7.67 (m, 6H), 7.75 (s, 2H), 7.779 (s, 2H), 7.782 (d, J = 8.4, 2H), 7.92 (d, J = 1.6, 2H). 13C NMR (101 MHz, CDCl3): 51.42, 55.00, 120.40, 120.87, 124.97, 125.23, 125.93, 127.30, 127.47, 128.33, 128.92, 131.90, 132.97, 138.37, 141.40, 143.34, 143.66. IR ($CHCl_3$): 3062 w, 3034 w, 2961 w, 2835 w, 1617 w, 1599 w, 1576 w, 1489 m,

1452 w, 1433 w, 1417 w, 1257 m, 1175 w, 1097 s, 1083 m, 905 m, 890 w, 699 m, 640 w, 570 w, 479 w cm^{-1}. APCI MS: 505 ($[M+H]^+$). HR APCI MS: calcd for $C_{37}H_{29}O_2$ 505.2162, found 505.2165.

15,15-Dimethoxy-2,10-diphenyl-6,13-dihydro-6,13-methanopentacene *meta*-Ph-A

A pressure tube was charged with *meta*-Br (200 mg, 0.39 mmol), phenylboronic acid (105 mg, 0.86 mmol, 2.2 equiv.), potassium carbonate (216 mg, 1.56 mmol, 4.0 equiv), Pd(PPh3)2Cl2 (14.0 mg, 0.02 mmol, 5 mol%), toluene (4 mL), ethanol (4 mL), and water (1 mL). The mixture was bubbled with nitrogen for 10 min and then it was heated to 85 °C and stirred at this temperature for 3 h. Then, the mixture was evaporated under reduced pressure and the residue was purified by flash chromatography on silica gel (hexane-ethyl acetate 100:1 to 20:1) to afford *meta*-Ph-A (169 mg, 86%) as a white amorphous solid.

^{1}H NMR (400 MHz, $CDCl_3$): 3.28 (s, 6H), 4.76 (d, J = 1.7, 1H), 4.77 (d, J = 1.7, 1H), 7.33 – 7.38 (m, 2H), 7.44 – 7.49 (m, 4H), 7.64 – 7.69 (m, 6H), 7.76 (s, 2H), 7.798 (d, J = 8.3, 2H), 7.800 (s, 2H), 7.93 (d, J = 1.6, 2H). 13C NMR (101 MHz, $CDCl_3$): 51.42, 54.99, 55.01, 120.37, 120.91, 124.96, 125.23, 125.94, 127.29, 127.47, 128.33, 128.92, 131.90, 132.96, 138.37, 141.40, 143.35, 143.65. IR (CHCl3): 3062 w, 3033 w, 2963 w, 2835 w, 1616 w, 1600 w, 1577 w, 1489 m, 1452 w, 1433 w, 1417 w, 1257 m, 1174 w, 1097 s, 1083 m, 905 m, 884 w, 699 m, 643 w, 552 w, 480 w cm^{-1}. APCI MS: 505 ($[M+H]^+$). HR APCI MS: calcd for $C_{37}H_{29}O_2$ 505.2162, found 505.2163.

2,9-Diphenyl-6,13-dihydro-6,13-methanopentacen-15-one *para*-Ph-C

A Schlenk flask was charged with *para*-A-Ph (100 mg, 0.20 mmol), flushed with nitrogen, and anhydrous dichloromethane (5 mL) was injected. Then trimethylsilyl iodide solution (1M in DCM, 240 µL, 0.24 mmol, 1.2 equiv) was added and the homogeneous reaction mixture was stirred overnight at rt. Then water (1 mL) was added and the mixture was stirred for 2 hours at rt. Then, sodium bisulfite (31.2 mg, 0.30 mmol, 1.5 equiv.) was added and the suspension was stirred for 10 min. The mixture was concentrated in vacuo and passed through the small pad of silicagel (eluent dichloromethane). The solvent was evaporated under vacuum to afford pure compound *para*-Ph-C (87 mg, 95 %) as a white solid. ^{1}H NMR (400 MHz, $CDCl_3$): 5.01 (s, 2H), 7.35 – 7.40 (m, 2H), 7.45 – 7.50 (m, 4H), 7.66 – 7.70 (m, 4H), 7.72 (dd, J = 8.5, 1.8, 2H), 7.87 (d, J = 8.3, 2H), 7.95 (s, 2H), 7.98 (s, 2H), 8.00 (d, J = 1.7, 2H). ^{13}C NMR (101 MHz, $CDCl_3$): not measured due to low solubility. IR (KBr): 3058 w, 3034 w, 1792 s, 1777 s, 1612 w, 1599 w, 1490 w, 1433 w, 1402 w, 1264 w, 1173 w, 1156 w, 1022 w, 911 m, 889 m, 879 m, 816 w, 770 m, 761 m, 698 m, 593 w, 471 m cm^{-1}. APCI MS: 431 ($[M-CO+H]^+$). HR APCI MS: calcd for $C_{34}H_{23}$ 431.1794, found 431.1793.

2,10-Diphenyl-6,13-dihydro-6,13-methanopentacen-15-one *meta*-Ph-C

A Schlenk flask was charged with *meta*-Ph-A (100 mg, 0.20 mmol), flushed with nitrogen, and anhydrous dichloromethane (5 mL) was injected. Then trimethylsilyl iodide solution (1M in DCM, 240 µL, 0.24 mmol, 1.2 equiv) was added and the homogeneous reaction mixture was stirred overnight at rt. Then water (1 mL) was added and the mixture was stirred for 2 hours at rt. After that, sodium bisulfite (31.2 mg, 0.30 mmol, 1.5 equiv.) was added and the suspension was stirred for 10 min. The mixture was concentrated in vacuo and passed through the small pad of silicagel (eluent dichloromethane). The solvent was evaporated under vacuum to afford pure compound *meta*-Ph-C (84 mg, 92 %) as a white solid. ^{1}H NMR (400 MHz, $CDCl_3$): 5.00 – 5.03 (m, 2H), 7.35 – 7.39 (m, 2H), 7.45 – 7.50 (m, 4H), 7.67 – 7.70 (m, 4H), 7.72 (dd, J = 8.4, 1.9, 2H), 7.87 (d, J = 8.3, 2H), 7.95 (s, 2H), 7.99 (s, 2H), 8.00 (d, J = 1.7, 2H). ^{13}C NMR (101 MHz, $CDCl_3$): not measured due to low solubility IR (KBr): 3038 w, 3034 w, 1791 s, 1776 s, 1612 w, 1598 w, 1490 w, 1433 w, 1403 w, 1263 w, 1173 w, 1156 w, 1022 w, 911 m, 888 m, 879 m, 816 w, 770 m, 761 m, 698 m, 593 w, 471 m cm^{-1}. APCI MS: 431 ($[M-CO+H]^+$). HR APCI MS: calcd for $C_{34}H_{23}$ 431.1794, found 431.1797.

OFETs characterization

The OFETs were characterized in dark at room temperature with a Karl Suss PA200 probe station and an Agilent 4145B using simultaneously source/measure units (SMU) and integrated measure units (VMUs). SMUs were connected to the gate, the drain and the source electrodes, while VMUs were used to monitor the channel voltage with the additional probes. Linear ($\mu_{TFT\text{-}lin}$) and saturation ($\mu_{TFT\text{-}sat}$) field effect mobilities were calculated based on the following equations. In the linear regime ($V_{DS} < V_{GS} - V_{th}$):

$$\mu_{TFT-lin} = g_m \frac{L}{W} \frac{1}{C_{SiO_2}.V_{DS}} \quad with\ g_m = \frac{\partial I_{DS}}{\partial V_{GS}} \qquad (Eq.1)$$

where W and L are the channel width and length respectively, C_{SiO2} is the oxide capacitance per unit area, V_{th} the threshold voltage and $\mu_{TFT\text{-}lin}$ the field effect mobility extracted via a linear fitting of the transconductance g_m.

For the saturation regime ($V_{DS} > V_{GS} - V_{th}$), $\mu_{TFT\text{-}sat}$, is extracted by linear fitting of the square root of I_{DS}:

$$\mu_{TFT-sat} = \frac{2L}{W} \frac{1}{C_{SiO_2}} \left(\frac{\partial \sqrt{|I_{DS}|}}{\partial V_{GS}} \right)^2 \qquad (Eq.2)$$

From transfer plots we extracted 4p field-effect mobilities by using the modified equation (1) in the linear regime incorporating the four-gate voltage and geometric parameters [38]:

$$\mu_{\mathrm{TFT-4p}} = \frac{D}{W} \frac{1}{C_{SiO_2}} \frac{\partial (I_{SD}.V_{4p})}{\partial V_{GS}} \qquad (Eq.3)$$

Where D is the center-to-center distance between the channel electrodes and V_{4p} the voltage between two probes along the corresponding section of the channel (see fig. SI-1).

Structural and morphological analysis

AFM observations were carried out using a Bruker AFM ICON. TEM investigations were performed under JEOL JEM 2100F – EDS operating under 120 kV at room temperature. GIXD investigations were conducted with a photon energy of 15 keV, and data was collected using a wide area plate image 2D X-pad detector (detector dimensions: 560 x 120 pixels, with a pixel size of 130 x 130 μm^2). The distance between the sample and the detector was 25 cm, which was calculated by measuring a LaB6 powder diffraction pattern. The incidence angle was optimized at 0.12°.

Supporting Information

Experimental procedures for the synthesis of 2,9- and 2,10-diphenylpentacene and their intermediates. NMR spectra, thermogravimetric and spectroscopic characterization, devices

schematic representation, additional devices electrical characteristics and AFM, TEM and GIXD results can be found in SI. The authors have cited additional references within the SI. [25,39]

Acknowledgements

Technical realizations were partly supported by the French RENATECH network. We are grateful to Nils Blanc, Gilbert Chahine and Maxime Dupraz for support during the experiment at ESRF beamline BM02 (Grenoble, France). The postdoc of MY Aliouat was supported by a FERMAT grant. Dr. Harald Bock is thanked for comments and corrections of the manuscript.

Keywords: acenes • charge mobility • nanostructures • organic electronics • organic field effect transistors

References:

[1] M. Watanabe, K.-Y. Chen, Y. J. Chang, T. J. Chow, *Acc. Chem. Res.* **2013**, *46*, 1606–1615.
[2] E. Busby, T. C. Berkelbach, B. Kumar, A. Chernikov, Y. Zhong, H. Hlaing, X.-Y. Zhu, T. F. Heinz, M. S. Hybertsen, M. Y. Sfeir, D. R. Reichman, C. Nuckolls, O. Yaffe, *J. Am. Chem. Soc.* **2014**, *136*, 10654–10660.
[3] S. N. Sanders, E. Kumarasamy, K. J. Fallon, M. Y. Sfeir, L. M. Campos, *Chem. Sci.* **2020**, *11*, 1079–1084.
[4] J. Lee, M. J. Bruzek, N. J. Thompson, M. Y. Sfeir, J. E. Anthony, M. A. Baldo, *Adv. Mater.* **2013**, *25*, 1445–1448.
[5] Z. Sun, Q. Ye, C. Chi, J. Wu, *Chem. Soc. Rev.* **2012**, *41*, 7857-7889.
[6] E. B. Guidez, C. M. Aikens, *J. Phys. Chem. C* **2013**, *117*, 21466–21475.
[7] K. Zhang, H. Wang, M. Fang, *Chem. Phys. Lett.* **2019**, *721*, 38–42.
[8] B. Purushothaman, S. R. Parkin, J. E. Anthony, *Org. Lett.* **2010**, *12*, 2060–2063.
[9] M. M. Payne, S. R. Parkin, J. E. Anthony, *J. Am. Chem. Soc.* **2005**, *127*, 8028–8029.
[10] J. Wang, M. Chu, J.-X. Fan, T.-K. Lau, A.-M. Ren, X. Lu, Q. Miao, *J. Am. Chem. Soc.* **2019**, *141*, 3589–3596.
[11] M. Chen, L. Yan, Y. Zhao, I. Murtaza, H. Meng, W. Huang, *J. Mater. Chem. C* **2018**, *6*, 7416–7444.
[12] J. Liu, H. Zhang, H. Dong, L. Meng, L. Jiang, L. Jiang, Y. Wang, J. Yu, Y. Sun, W. Hu, A. J. Heeger, *Nat. Commun.* **2015**, *6*, 10032.
[13] W. Xu, Y. He, I. Murtaza, D. Zhang, A. Li, Z. Hu, X. Zeng, Y. Guo, Y. Zhu, M. Liu, H. Meng, *J. Mater. Chem. C* **2017**, *5*, 2852–2858.
[14] A. N. Aleshin, J. Y. Lee, S. W. Chu, J. S. Kim, Y. W. Park, *Appl. Phys. Lett.* **2004**, *84*, 5383–5385.
[15] J. Liu, H. Dong, Z. Wang, D. Ji, C. Cheng, H. Geng, H. Zhang, Y. Zhen, L. Jiang, H. Fu, Z. Bo, W. Chen, Z. Shuai, W. Hu, *Chem. Commun.* **2015**, *51*, 11777–11779.
[16] D. J. Gundlach, J. A. Nichols, L. Zhou, T. N. Jackson, *Appl. Phys. Lett.* **2002**, *80*, 2925–2927.
[17] C. Reese, W.-J. Chung, M. Ling, M. Roberts, Z. Bao, *Appl. Phys. Lett.* **2006**, *89*, 202108-1.
[18] H. Chang, W. Li, H. Tian, Y. Geng, H. Wang, D. Yan, T. Wang, *Org. Electron.* **2015**, *20*, 43–48.
[19] W. Xie, K. A. McGarry, F. Liu, Y. Wu, P. P. Ruden, C. J. Douglas, C. D. Frisbie, *J. Phys. Chem. C* **2013**, *117*, 11522–11529.
[20] H. Klauk, M. Halik, U. Zschieschang, G. Schmid, W. Radlik, W. Weber, *J. Appl. Phys.* **2002**, *92*, 5259–5263.
[21] O. D. Jurchescu, J. Baas, T. T. M. Palstra, *Appl. Phys. Lett.* **2004**, *84*, 3061–3063.
[22] M. Watanabe, Y. J. Chang, S.-W. Liu, T.-H. Chao, K. Goto, Md. M. Islam, C.-H. Yuan, Y.-T. Tao, T. Shinmyozu, T. J. Chow, *Nat. chem.* **2012**, *4*, 574–578.
[23] T. Miyazaki, M. Watanabe, T. Matsushima, C. Chien, C. Adachi, S. Sun, H. Furuta, T. J. Chow, *Chem.-Eur. J.* **2021**, *27*, 10677–10684.
[24] E. Bedel Pereira, J. Bassaler, H. Laval, J. Holec, R. Monflier, F. Mesnilgrente, L. Salvagnac, E. Daran, B. Duployer, C. Tenailleau, A. Gourdon, A. Jancarik, I. Séguy, *RSC Adv.* **2022**, *12*, 671–680.
[25] G. Levet, N. K. Hung, M. Šámal, J. Rybáček, I. Cisařová, A. Jancarik, A. Gourdon, *Eur. J. Org. Chem.* **2020**, *11*, 1658–1664.
[26] T. Aotake, S. Ikeda, D. Kuzuhara, S. Mori, T. Okujima, H. Uno, H. Yamada, *Eur. J. Org. Chem.* **2012**, *9*, 1723–1729.
[27] H. H. Choi, K. Cho, C. D. Frisbie, H. Sirringhaus, V. Podzorov, *Nat. Mater.* **2018**, *17*, 2–7.
[28] K. P. Puntambekar, P. V. Pesavento, C. D. Frisbie, *Appl. Phys. Lett.* **2003**, *83*, 5539–5541.
[29] K. Kim, E. J. G. Santos, T. H. Lee, Y. Nishi, Z. Bao, *Small* **2015**, *11*, 2037–2043.
[30] L. F. Drummy, P. K. Miska, D. C. Martin, *J. Mater. Sci.* **2004**, *39*, 4465–4474.
[31] H. Qian, M. Malac, R. Egerton, *Philos. Mag.* **2007**, *87*, 253–266.
[32] H. Qian, R. Egerton, M. Malac, *Microsc. Microanal.* **2005**, *11*, 2044-2045.
[33] T. A. Dramstad, Z. Wu, G. M. Gretz, A. M. Massari, *J. Phys. Chem. C* **2021**, *125*, 16803–16809.
[34] T. Kakudate, N. Yoshimoto, Y. Saito, *Appl. Phys. Lett.* **2007**, *90*, 081903.
[35] M. Klues, G. Witte, *CrystEngComm* **2018**, *20*, 63–74.
[36] S. CB. Mannsfeld, A. Virkar, C. Reese, M. F. Toney, Z. Bao, *Adv. Mater.* **2009**, *21*, 2294–2298.
[37] H. -L. Cheng, Y. -S. Mai, W. -Y. Chou, L. -R. Chang, X. -W. Liang, *Adv. Funct. Mater.* **2007**, *17*, 3639–3649.
[38] C.-Y. Chen and J. Kanicki, IEEE Electron Device Lett. **1997**, 18, 340-342.
[39] G. Levet, N.K. Hung, M. Šámal, J. Rybáček, I. Cisařová, A. Jancarik, A. Gourdon, *Eur. J. Org. Chem.* **2020**, *11*, 1620-2008

Entry for the table of contents

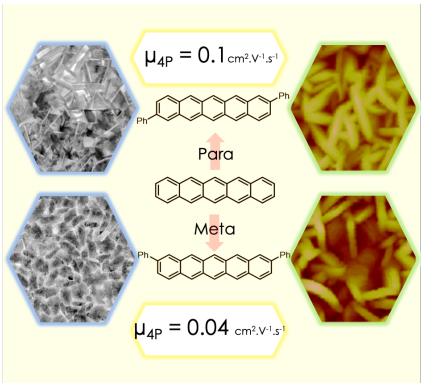

Exploring morphological structures of new β-Disubstituted pentacene derivatives: TEM optical micrographs and AFM topographies unveil the impact of chemical structure on 4-probe field effect hole mobilities.